Full Length Article

Ab initio simulation of the dynamic shock response of single crystal and lightweight multicomponent alloy

Yulun Xu [a], Wenguang Nan [a,*], Zhonggang Sun [b]

[a] School of Mechanical and Power Engineering, Nanjing Tech University, Nanjing 211816, China
[b] College of Materials Science and Engineering, Nanjing Tech University, Nanjing 211816, China

ARTICLE INFO

ABSTRACT

The dynamic response of shock wave impact on single crystal aluminium and lightweight multicomponent alloy Al-Cu-Li-Mg is simulated by using the combination of Ab initio Molecular Dynamics (AIMD) and Multi-Scale Shock Technique (MSST), with the analysis carried out at the atomic/electronic levels. The simulation is verified by comparing the particle velocity of single crystal obtained in this work with the data in literature. The shock compression process not only involves the migration of atoms, but also is related to electronic transition. Two stages could be found in the shock compression process: oscillatory compression of the crystal cell and oscillatory migration of the atoms. The crystal structure of the multicomponent alloy could be disordered even at low shock speed, due to the difference in the ability to migrate between different kinds of atoms. As the sample is shock-compressed, the contribution proportion of crystal orbitals shows a sharp decrease for D orbital, while it increases significantly for S orbital and P orbital. The electron structure shows a quicker response to the shock wave compression process than the crystal structure. The orbital contribution from P orbital of the crystal is mainly due to the P orbital of Al atoms, while the orbital contribution from D orbital of the crystal is mainly due to the D orbital of Cu atoms. Total Density of States (TDOS) is mainly contributed by the Projected Density of State (PDOS) of Cu atoms in the occupied state of energy levels, while it is close to the PDOS of Al atoms in the non-occupied state of energy levels.

1. Introduction

Multicomponent alloy have a number of advantages over traditional metals, such as exhibiting more excellent mechanical behaviour and higher strength properties [1], making them potentially useful in a variety of applications, especially for impact-resistant materials under extremely high strain rate deformation [2], i.e. shock compression, such as aerospace structural components and armour defence product [3], high-pressure equipment [4]. The behaviour of multicomponent alloys under shock compression has been studied by various researchers [5–10], in which the effects of the shock rate as well as types of elements are highlighted. However, there is not limited work on the shock dynamics of lightweight multicomponent alloy, especially the ones with aluminium element, which recently gained more and more interest [11] due to maintaining good mechanical properties while significantly reducing weight. The roles of the aluminium element and other kinds of elements during the shock compression process have not been well understood.

To explore the shock dynamics of multicomponent alloy under shock and impact compression, nonequilibrium molecular dynamics (NEMD) has been used by several researchers [12–18] due to its ease of use. In this method, specified velocities are applied to a layer of atoms or molecules at the boundary of the simulation box, and these atoms or molecules further impact their neighbours through interatomic interactions, leading to the propagation of the applied velocity profile through the material and the formation of shock wave with a sudden increase in pressure and temperature. By using NEMD simulation, Xie et al. [13] investigated the shock response and corresponding deformation mechanism of medium entropy alloy CoCrNi, and they found that the lattice distortion could decrease the barrier for dislocation nucleation. Similarly, Liu et al. [14] studied the shock-induced deformation of CoCrFeMnNi alloy, and their results showed that the plasticity mechanisms depended on the crystallographic orientation. Zhao et al. [16] investigated the dislocation structure behind the shock-wave front in bcc high-entropy alloy, and they showed that it was due to the low elastic stability of local structure of the alloy. Compared to NEMD, the

coupling of Multi-Scale Shock Technique (MSST) [19] with molecular dynamics (MD) is another method to model the shock compression of materials with several advantages, such as low computational cost, good flexibility such as the ability to model the shock propagating in any directions. In this method, a one-dimensional compressible flow governed by the Euler equations is employed in MSST to track the propagation of the shock front, determining properties such as pressure, temperature, and velocity, while MD dynamically adjusts the positions and velocities of individual atoms or molecules based on the information received from MSST. Therefore, more detailed information at both the atomic and molecular scales could be obtained, i.e. the macroscopic perspective provided by MSST with the detailed atomic-level insights offered by MD, enables a more comprehensive understanding of shock wave phenomena and material behavior under extreme conditions. Recently, several researchers [20–24] applied MD-MSST simulation to the shock compression of multicomponent alloy, although lightweight multicomponent alloys are rarely involved. For example, Chen et al. [20] investigated the low-temperature shock behaviour of CoCrFeMnNi alloy, and they found that the void structure within the alloy promoted the formation of dislocations and defects at lower piston/shock speeds. Similarly, Singh et al. [22] simulated the deformation of CoCrCuFeNi alloy subjected to shock loading, and their results showed that the size of the grain significantly affected the shock response.

However, in both NEMD and MD-MSST simulations, the interatomic potential is necessarily assumed in advance to quantify the interaction forces between different kinds of elements of the multicomponent alloy, which is usually difficult to be accurately obtained or available in the literature, especially for newly developed multicomponent alloy. On the other hand, the coupling of Ab initio Molecular Dynamics (AIMD) with MSST has been developed to investigate the shock behaviour of materials at the atomic/electronic levels [25–27], in which the interaction between different elements is directly calculated from first-principles such as density functional theory (DFT) [28,29] without assuming the interatomic potential as the NEMD and MD-MSST simulations. Therefore, by using AIMD-MSST simulation, the shock dynamics of materials could be more accurately modelled, especially at the atomic and electronic levels. For example, by using AIMD-MSST simulation, Mundy et al. [25] simulated the shock-induced phase transformation of graphite to diamond, and they found that a new intermediate layered diamond phase could be formed without plane sliding, through the buckling of basal planes. Similarly, Neogi et al. [27] carried out the shock simulation of Cu using different shock-intensities and different orientations of the lattices, and their results agreed well with in-situ real-time XRD diffraction analysis. However, till now, according to the authors' knowledge, there is almost no research to apply this method to explore the shock compression of multicomponent alloy, especially for lightweight multicomponent alloy, but it is highly desirable for an accurate and comprehensive understanding of the shock behaviour, especially at both atomic and electronic levels.

In this work, the coupling of Ab initio Molecular Dynamics (AIMD) and Multi-Scale Shock Technique (MSST) is applied to the modelling of shock dynamics of lightweight multicomponent Al-Li-Cu-Mg alloy, in which single crystal aluminium is also involved for comparison. Effects of shock speed on the compression dynamics, atomic migration and electron structure are focused. This provides a further step towards better understanding of the performance of lightweight multicomponent alloy under shock compression, and further seeking of the potential of AIMD in the research of lightweight multicomponent alloy at the atomic/electronic levels.

2. Methods

In this work, the coupling of Ab initio Molecular Dynamics (AIMD) and Multi-Scale Shock Technique (MSST) is used to simulate the behaviour of metal materials under shock compression with atomic-level accuracy, by using the latest open-source CP2K software package

[30]. Its calculation principles and flowchart are schematically illustrated in Fig. 1. Based on the information of the initial crystal structure (such as specific volume and temperature) and the shock speed (V_s), the propagation of shock wave is calculated by MSST, obtaining the constraints on the AIMD system, such as the shock-induced changes in specific volume and temperature. Afterwards, the electronic structure calculation using Density Functional Theory (DFT) is performed to obtain the electronic energy and wave function, and then molecular dynamics calculation is conducted to evolve the system over time, considering both electronic and ionic motions. By exchanging the information between the AIMD and MSST simulations at specified intervals, i.e. shock conditions of crystal structure (such as specific volume and temperature) form AIMD, system constraints on AIMD from MSST, the complex interplay between electronic and atomic dynamics and shock wave propagation is simulated until the desired simulation time is reached. The visualisation and analysis of the shock compression process is carried out by using Visual Molecular Dynamics (VMD) [31] and Multiwfn software package [32,33].

In AIMD, Density Functional Theory (DFT) is used to describe the electronic structure and interatomic interactions within a material accurately, accounting for both electronic and atomic motions and allowing for the investigation of dynamic processes at the atomic level. MSST provides constraints on AIMD simulations by calculating shock-induced changes in material properties such as specific volume and temperature.

For the coupling between AIMD and MSST, exchange information between the AIMD and MSST simulations at appropriate intervals or time steps. Update the AIMD simulation parameters based on the constraints obtained from the MSST calculation. This could include adjusting the volume, temperature, or other relevant parameters to account for the effects of the shock wave. Incorporate the shock-induced changes into the AIMD simulation by modifying the potential energy surface or other relevant parameters to accurately represent the evolving system.

2.1. Multi-Scale shock Technique (MSST)

Following the method proposed by Reed et al. [19], the propagation of the shock wave is modelled by using one-dimensional Euler equations of compressible flow, including the conservation equations of mass, momentum and energy. The stress of the AIMD system in the propagation direction is constrained to the Rayleigh line, while the energy of the AIMD system is constrained to the Hugoniot relation, given as [19]:

$$V_p = V_s(1 - \frac{\rho_0}{\rho}) \tag{1}$$

$$P - P_0 = V_s^2 \rho_0 (1 - \frac{\rho_0}{\rho}) \tag{2}$$

$$e - e_0 = P_0(\frac{1}{\rho_0} - \frac{1}{\rho}) - \frac{V_s^2}{2}(1 - \frac{\rho_0}{\rho})^2 \tag{3}$$

where P is the shock pressure, i.e. the negative component of the stress tensor in the direction of shock propagation, (i.e. X-direction); V_s is the shock speed; V_p is the particle velocity; $\rho = 1/v$ is the density, with v being the specific volume; e is the energy per unit mass. P_0, e_0, and ρ_0 refers to the corresponding input parameter. These equations are applied to the system which has a time-independent steady state in the reference frame moving at the shock speed V_s. The specific volume v ($1/\rho$) in these equations for AIMD simulation is given as:

$$Q\frac{\partial^2 v}{\partial t^2} = \frac{\partial K}{\partial v} - \frac{\partial V}{\partial v} - P_0 - \frac{V_s^2}{v^2}(v_0 - v) \tag{4}$$

where K and V are the kinetic and potential energies per unit mass, respectively; Q is a mass-like parameter for the simulation cell size. $v_0 =$
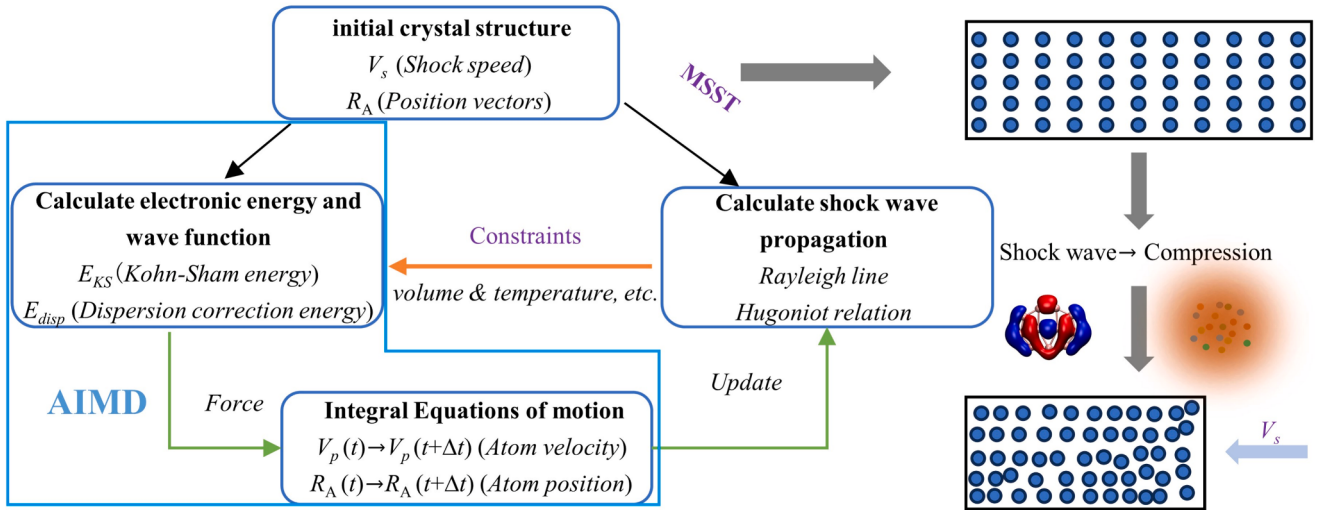
Fig. 1. Computational principles of shock wave shock compression process.

$1/\rho_0$ is the specific volume at the pre-shocked state. It should be noted that the strain is allowed only in the shock direction. Based on Eqs. (2)-(4), the properties of the system corresponding to the material undergoing a shock with wave speed of V_s, i.e. temperature, pressure, and the particle velocity (i.e. local speed of the material in the laboratory frame), could be obtained after sufficient equilibration. More information of MSST could be referred to Reed et al. [19].

2.2. Ab initio Molecular dynamics (AIMD)

The key of AIMD is the density functional theory (DFT), and thus it is detailed described here. DFT is a theoretical framework used to describe and calculate the electronic structure and properties of atoms, molecules, and solid materials. By solving the Kohn-Shan equations, a self-consistent set of single-electron wave functions and energy levels can be obtained. This allows for the calculation of various physical and chemical properties related to electronic structure, including energy, charge distribution, electron orbitals, and other relevant characteristics [34–36]. Due to the computational characteristics of wave functions, standard density functional approximations usually cannot well describe the long-range London dispersion interactions. These dispersion interactions usually play a crucial role in the formation of large structures. Therefore, introducing dispersion correction methods can significantly improve the accuracy of calculations [28,29,34].

Here, DFT-D3 in CP2K software package is used, which is an empirical correction method designed to account for the dispersion correction or van der Waals interactions in density functional theory, and thus it can significantly improve the accuracy of simulation and calculation using DFT [37]. In the DFT-D3 scheme, the total energy E_{tot} of the system is the sum of the Kohn-Shan energy E_{KS} and the dispersion correction E_{disp}, given as [38]:

$$E_{tot} = E_{KS} + E_{disp} \qquad (5)$$

where E_{disp} is the cumulative energy contribution from all individual attractive atom pairs (e.g. atom A and atom B), and it is dependent on the nth order dispersion coefficients C_n^{AB} and the atomic distance R_{AB}. As odd n and other interaction effects are usually neglected, E_{disp} is given as:

$$E_{disp} = -\sum_{AB} \sum_{n=6,8,10,\dots} \frac{C_n^{AB}}{R_{AB}^n} f_{damp}(R_{AB}, A, B) \qquad (6)$$

where the leading term with $n = 6$ is included to ensure the accuracy of asymptotic behaviour of the potential; f_{damp} is the damping function, and it is used to avoid the singularities at small distances and double

counting of electron correlation at medium distances.

Based on the Hohenberg-Kohn theorem [28] and the Kohn-Shan equations [29], the ground-state properties of a system can be determined by minimizing the total energy functional, in which the electronic KS energy functional E_{KS} is given as [39]:

$$E_{KS}[\{\phi_i\}] = T_s[\{\phi_i\}] + \int V_{ext}(r)n(r)dr + \frac{1}{2}\int V_H(r)n(r)dr + E_{XC}[n] \qquad (7)$$

where ϕ_i is the Kohn–Shan orbitals; T_s is the kinetic energy of electrons; $V_{ext}(r)$ is the Coulomb interaction between electrons and nuclei; $V_H(r)$ is Hartree potential, and the corresponding integration is the total electrostatic (Coulomb) energy; E_{XC} is the exchange–correlation energy functional; $n(r)$ is the electron density, which could be obtained from a single slater determinant (i.e. Kohn–Shan determinant) and built from the occupied orbitals, given as:

$$n(r) = \sum_i^{occ} f_i|\phi_i(r)|^2 \qquad (8)$$

where f_i is integer occupation number.

2.3. Simulation conditions

In this work, the single crystal aluminium and aluminium-rich multicomponent alloy are used. After the structural optimisation of the crystal cell, the thermodynamic equilibrium is relaxed by 1 ps at 300 K through NPT ensemble. Periodic boundary conditions (PBC) are maintained in all three orthogonal directions during the pre-equilibrium period. Then the simulation of the shock compression process is carried out. The shock wave propagates only in the X-direction (i.e. a direction of the crystal cell), which provides a uniaxial strain condition. For the single crystal aluminium, the simulated sample is composed of 256 atoms, corresponding to $4 \times 4 \times 4$ crystal lattice units, with the size ($a \times b \times c$) of 16.2 Å $\times$ 16.2 Å $\times$ 16.2 Å, and the shock wave speeds of 9 km/s, 10 km/s and 12 km/s are used. For the aluminium-rich multicomponent alloy, Al-Li-Cu-Mg reported by Pavlyuk et al. [40] is considered here, and the simulated sample consists of 324 atoms, i.e. Al168 Cu52 Li80 Mg24, with the lattice parameters of $a = 27.6$ Å, $b = 13.8$ Å and $c = 13.8$ Å, and the simulated samples were constructed from Multiwfn, while three kinds of shock speeds are used, i.e. 8 km/s, 10 km/s and 12 km/s.

The total AIMD simulation time is 1 ps, with a time step of 0.2 fs. The same basis group (MOLOPT) and pseudopotential (GTH) are used in structural optimisation, pre-equilibrium and dynamics modelling of shock compression. The generalized gradient approximate functional

Perdew-Burke-Ernzerhof (PBE) is used. The single crystal aluminium system with the cutoff of 400 Ry is used. Meanwhile, due to the complexity and large energy of the aluminium-rich multicomponent alloy system considered in this work, the cutoff of 800 Ry is then used to improve the calculation accuracy. The initial volume, pressure, and energy of the AIMD process are calculated from the pre-equilibrium. Because the magnetic properties of the atoms in the system are very weak, and the copper is often diamagnetic under normal conditions, thus, the effect of the magnetic moment on the system is not considered in this work.

3. Results and discussions

3.1. Single crystal aluminium

The variation of calculated particle velocity with pre-set shock speed is shown in Fig. 2, where the data in previous work is also included, i.e. Mitchell et al. [41], Choudhuri et al. [42], Yang et al. [43], Ju et al. [44]. It is clearly that there exists a linear relationship between particle velocity and shock speed. Meanwhile, the data in this work agrees well with both the experimental result in Mitchell et al. [41], and the numerical data in Choudhuri et al. [42], Yang et al. [43] and Ju et al. [44]. Variation of the pressure with the volume ratio is shown in Fig. 3, where the data in previous work is also included, i.e. Mitchell et al. [41], Nellis et al. [45], Yang et al. [43], Ju et al. [44]. A good agreement between this work and previous work could be found.

The final thermodynamic state at different shock speeds is summarised in Table 1. At the shock speed of 9 and 10 km/s, the thermodynamic temperature is 1300 K and 1750 K, respectively, while the corresponding pressure is 68 GPa and 103 GPa. Based on experimental data of aluminium samples obtained from Lomonosov [46], it could be found the thermodynamic temperature in these cases is below the shock melting point (i.e. 3000 K at 70 GPa, and 3900 K at 100 GPa). However, at the shock speed of 12 km/s, the temperature could suddenly increase to 6250 K, which exceeds the shock melting point (i.e. 4600 K at 165 GPa). Under this condition, the compression of single crystal aluminium may lead to a disordered structure. As shown in Table 1, with the increase of the shock speed, the kinetic energy and the pressure (i.e. component of the stress tensor in the compression direction) at the equilibrium state show a similar trend as that of the temperature, while the lattice size of the crystal cell in the compression direction only shows a slight decrease.

The atomic coordinates are further visualized by VMD software package [31], and the migration trajectory of atoms during the shock
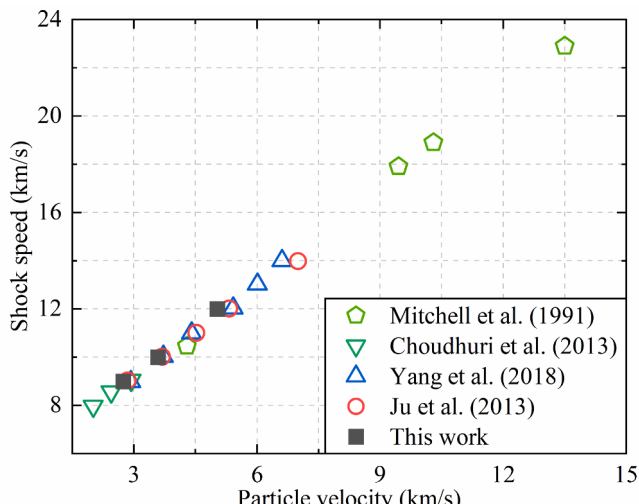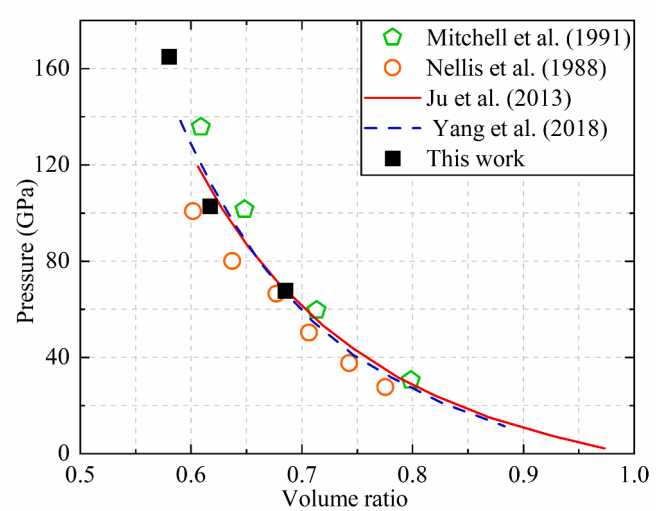
Fig. 3. Variation of the pressure with the volume ratio, which is calculated as the ratio of after-shock volume to the pre-shock volume.

Table 1
Final thermodynamic state of single crystal at different shock speeds.

Parameters	$V_s = 9$ km/s	$V_s = 10$ km/s	$V_s = 12$ km/s
Temperature (K)	1300	1750	6250
Pressure (GPa)	68.0	103.1	165.2
Kinetic energy (a.u.)	1.5	2.1	7.5
Lattice size a (Å)	11.1	10.1	9.4

compression process is shown in Fig. 4. The compression process of the sample could be divided into two stages: oscillatory compression of the crystal cell, and oscillatory migration of the atoms. At $t = 0.2$ ps, the sample is already compressed for all cases, and the compression is in the first stage, i.e. the crystal cell is in the period of compression-bouncing. At the shock speed of 9 km/s and 10 km/s, the first period of compression-bouncing has not been finished, while the shock front has already bounced back at the shock speed of 12 km/s. The compression extent of the crystal cell at the shock speed of 12 km/s is the largest, which is intuitively expected. The oscillatory migration of atoms is in the time interval between 0.4 ps and 1 ps for all shock speeds considered in this work. As the temperature during the compression process is always below the boiling point at the shock speed of 9 km/s and 10 km/s, the oscillatory migration of atoms is almost ordered. However, at the shock speed of 12 km/s, the temperature is far beyond the boiling point, making compressed crystal melted or even vaporised. Correspondingly, the oscillatory migration of atoms is in a disordered style, and some atoms even run out of the crystal cell.

Table 2 shows the contribution proportion of atomic orbitals to the crystal orbitals (CO) at the initial state and final state after compression, in which No. 200 occupied orbital is analysed by using the Multiwfn program with Ros-Schuit (SCPA) partition [32,33]. At the initial state, the contribution proportion of S orbital and P orbital is 41.5 % and 54.9 %, respectively, while only a small amount of the orbitals are contributed by D orbital. However, after shock compression, the orbital distribution of the crystal is significantly changed. At the shock speed of 9 km/s, the contribution proportion of P orbital increases to 68.0 % while the contribution proportion of S orbital decreases to 26.1 %, but the contribution proportion of the D orbital remains almost unchanged. As the shock speed further increase to 12 km/s, the contribution proportion of S orbital shows an increase. This maybe due to the electronic transition during the compression process, i.e. the transition of electrons from the occupying orbitals to the non-occupying orbitals. Therefore, the shock compression process of single crystal not only involves the


Fig. 2. Variation of the calculated particle velocity with pre-set shock speed.
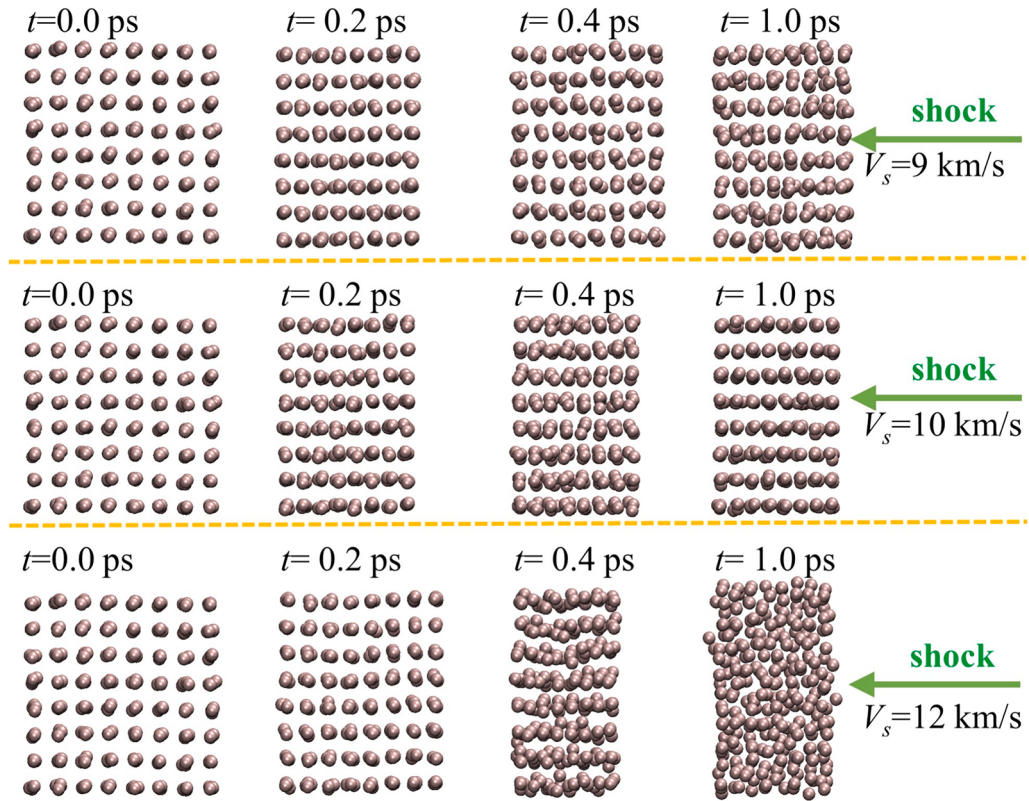
Fig. 4. Migration of atoms of single crystal under different shock speeds.

Table 2
Orbital contribution proportion of No. 200 occupied orbital of single crystal.

Shock speed	S orbital	P orbital	D orbital
Initial state	41.5 %	54.9 %	3.6 %
$V_s = 9$ km/s	26.1 %	68.0 %	5.8 %
$V_s = 10$ km/s	28.2 %	65.7 %	6.1 %
$V_s = 12$ km/s	39.5 %	55.3 %	5.1 %

migration of atoms, but also is related to electronic transition.

3.2. Lightweight multicomponent alloy

Fig. 5 shows the variation of the thermodynamic parameters of the sample with time during the shock compression process, including the temperature and pressure, and Table 3 summarises the thermodynamic parameters at the final state after compression (Same as Table 1). As shown in Fig. 5(a), the temperature starts to increase at about 0.25 ps for all three cases, indicating that the compression of the crystal cell occurs after 0.25 ps. It is much later than that of the single crystal aluminium, as shown in Fig. 4, in which the sample has already been compressed at 0.2
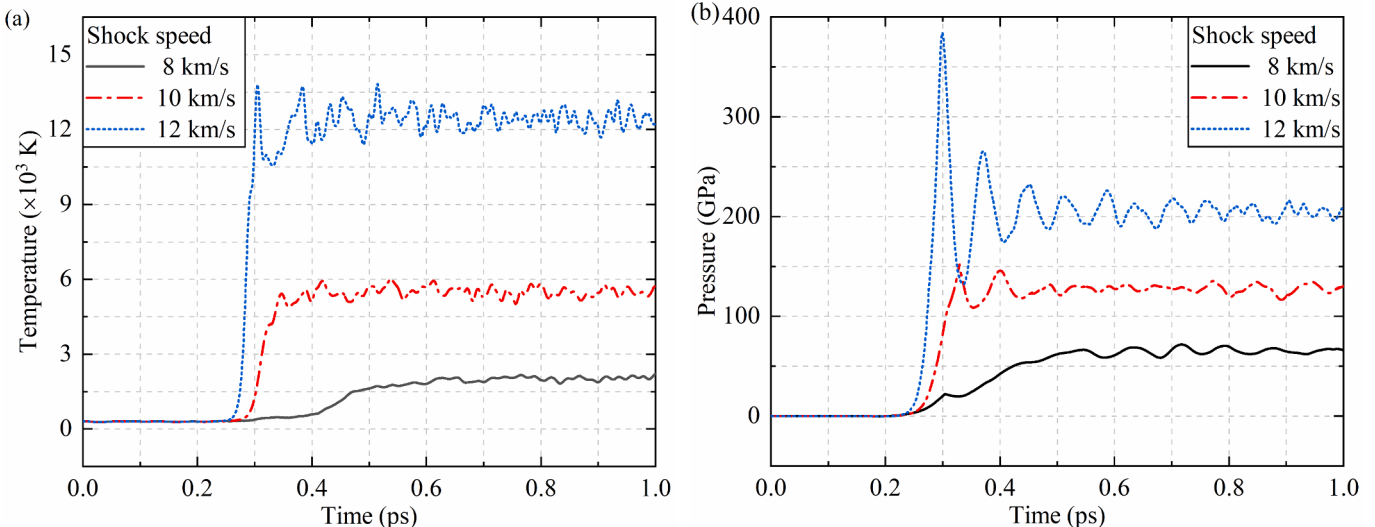
Fig. 5. Variation of the thermodynamic parameters of the sample with time during the shock compression process: (a) temperature; (b) pressure.

Table 3
Final thermodynamic state of Al-Li-Cu-Mg alloy at different shock speeds.

Parameters	$V_s = 8$ km/s	$V_s = 10$ km/s	$V_s = 12$ km/s
Temperature (K)	2050	5500	12400
Pressure (GPa)	65.0	128.0	205.4
Kinetic energy (a.u.)	3.2	8.4	19.0
Lattice size a (Å)	21.5	15.1	13.5

ps. It demonstrates that the multicomponent alloy has more resistance to shock compression than that of the single crystal aluminium, which is intuitively expected. Then the temperature increases quickly to the value close to the equilibrium state and fluctuates around it. With the increase of the shock speed, the temperature would increase more quickly with time and reach the equilibrium state in a shorter time. For example, after 0.25 ps, the temperature reaches the equilibrium value in only $\Delta t = 0.05$ ps for the shock speed of 12 km/s, while it takes about $\Delta t = 0.25$ ps for the shock speed of 8 km/s. It should be noted that the temperature at the shock speed of 8 km/s is always below the boiling point, resulting in a slow response to the shock compression. Correspondingly, as shown in Table 3, the final thermodynamic temperature is 2050 K, 5500 K and 12400 K for the shock speeds of 8 km/s, 10 km/s and 12 km/s, respectively. As shown in Fig. 5(b), the variation of the pressure (i.e. the component of the stress tensor in the compression direction) with time is similar to that of the temperature, i.e. starts to increase at 0.25 ps, and then increases quickly to the maximum value and fluctuates around the equilibrium state, with the amplitude of the fluctuation decreasing with time. It should be noted that when the pressure reaches the maximum, the compression of the sample is actually completed, and then the shock front oscillates, i.e. bouncing and compression. With the increase of the shock speed, the oscillation would be larger, which is intuitively expected. Correspondingly, as summarised in Table 3, the equilibrium pressure at the shock speed of 8 km/s, 10 km/s and 12 km/s are 65.9 GPa, 128.0 GPa and 205.4 GPa, respectively. It is obviously that at the shock speed of 8 km/s, the equilibrium pressure is much smaller than that of other two shock speeds, which is due to that the whole compression process is below the boiling point. Table 3 also

shows that with the increase of the shock speed, the kinetic energy at the final state increases sharply, while the extent of the compression changes slightly, as indicated by the lattice size of the crystal cell in the compression direction. For example, as the shock speed increases from 8 km/s to 10 km/s, the kinetic energy almost increases 2.5 times, while the lattice size a decrease only from 21.5 Å to 15.1 Å.

Fig. 6 shows the migration trajectories of the atoms during the shock compression process. At $t = 0.2$ ps, as the system does not show any compression, similar structure is observed for all shock speeds. By comparing the spatial positions of atoms between 0.4 ps and 1.0 ps, it is clearly that the compression process at 0.4 ps is not finished at the shock speed of 8 km/s while it almost enters the equilibrium state with the oscillation of atoms at the shock speed of 10 km/s and 12 km/s. This agrees well with the variation of the temperature and pressure with time shown in Fig. 5. It is interesting that at the shock speed of 10 km/s, some atoms migrate outside the crystal cell. This may be due to that the corresponding temperature during the compression process is too high, as shown in Fig. 5(a). Under this condition, the crystal is partially melted or vaporised, resulting in significantly disordered migration of some atoms, in which the migration amplitude of the lithium atoms is the largest among all atoms. When the shock speed increases to 12 km/s, a large number of atoms migrate outside the crystal cell, resulting in larger disordered distribution of atoms, as the crystal is completely melted or vaporised. It is consistent with the extremely high thermodynamic temperature shown in Table 3. It should be noted that even at the shock speed of 8 km/s, the crystal after compression also shows a disordered cluster, although the extent of disorder is much smaller than that of the shock speed of 10 km/s and 12 km/s.

To illustrate the structure of the crystal cell after compression, the Radial distribution function (RDF) of the Al atoms is calculated by averaging the data in last 0.5 ps, as shown in Fig. 7(a). For comparison, the RDF of crystal cell at the initial state is also included, in which the peaks could be clearly observed with the first peak at about 2.6 Å, indicating that the crystal structure is ordered. After shock compression, the first peak shifts to left, and other peaks become less clear and almost disappear, especially for large shock speed. It demonstrates that the

(a) V_s =8 km/s   (b) V_s =10 km/s   (c) V_s =12 km/s
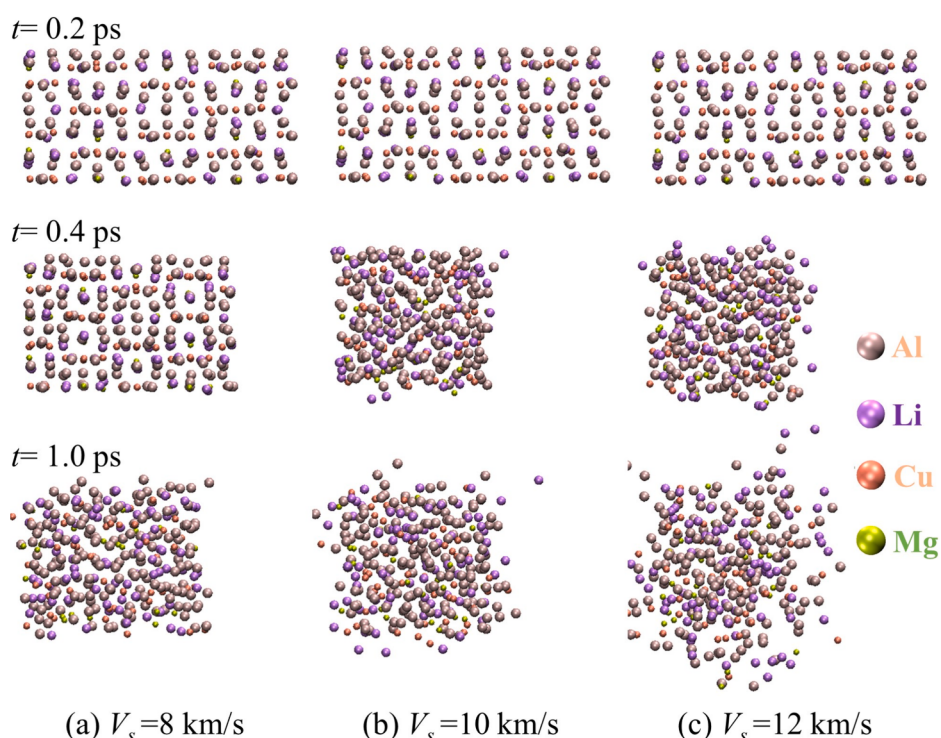
Fig. 6. Migration of atoms of Al-Li-Cu-Mg alloy under different shock speeds.
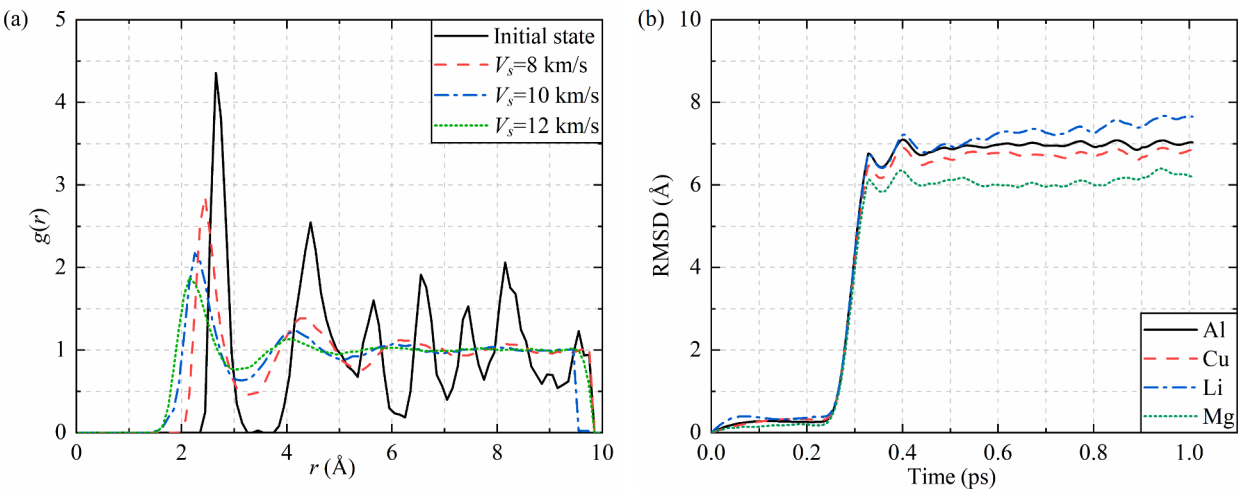
Fig. 7. Characteristics of crystal structure: (a) Radial Distribution Function of Al-Al at different shock speeds, and (b) Root-Mean-Square Displacement of each atom at the shock speed of 10 km/s.

crystal changes from initially ordered structure to a disordered structure. Meanwhile, Fig. 6 also shows that the migration of Mg atoms and Cu atoms shows an aggregation phenomenon, while the Al atoms and Li atoms tend to migrate outside. To further illustrate underlying mechanism, the Root Mean Square Displacement (RMSD) is analysed based on the trajectories of atoms in Fig. 6(b), as shown in Fig. 7(b). It is found that Li atoms have a much stronger diffusion capacity than that of Mg atoms during the oscillation of compression. It demonstrates again that the Li atoms are more easily to migrate outside the crystal cell under the compression of shock wave.

The electronic structure of the sample at the equilibrium state is also analysed here, following the same method of single crystal aluminium in Section 3.1. As the system is too large, only half of the crystal cell is used during the calculation. Here, the No. 300 occupied orbital with an energy of -3.1 eV at the initial state is used for analysis, which is close to the highest occupied crystal orbital (HOCO). Compared to other crystal orbitals, the electronic structure on the No. 300 occupied orbital shows more significant changes during the shock compression process of the sample. By calculating the basis function contribution of No. 300 occupied crystal orbital, it is found that the orbital contribution mainly comes from S orbital, P orbital and D orbital, with a total contribution proportion of 99.9 %. Table 4 and Table 5 summarise the contribution proportion of crystal orbital of the sample at the initial and final states, and Fig. 8 shows the variation of corresponding contribution proportion with time. As shown in Table 4, the crystal orbital at the initial state is mainly contributed by D orbital with a contribution proportion of 90.7 %, while the contribution proportion of S orbital and P orbital is only 3.7 % and 5.5 %, respectively. This is much different to that of single crystal aluminium shown in Table 2. It is mainly due to the existence of Cu atoms in the multicomponent alloy, as the contribution of atoms to the crystal orbital at the initial state is mainly from Cu atoms, as shown in Table 5 and Fig. 8. At the shock speed of 8 km/s, as the sample is compressed, the contribution proportion shows a sharp decrease for D orbital, while it increases sharply for S orbital and P orbital. It is interesting that even at 0.2 ps, the contribution proportion is much different

Table 4
Atomic contribution to the crystal orbitals of No. 300 occupied orbital of Al-Li-Cu-Mg alloy.

Shock speed	S orbital	P orbital	D orbital
Initial state	3.7 %	5.5 %	90.7 %
$V_s =$ 8 km/s	21.7 %	17.1 %	61.1 %
$V_s =$ 10 km/s	33.1 %	31.1 %	35.7 %
$V_s =$ 12 km/s	44.5 %	26.4 %	29.0 %

Table 5
Contribution of atoms to the crystal orbitals of No. 300 occupied orbital of Al-Li-Cu-Mg alloy.

Shock speed	Al	Li	Cu	Mg
Initial state	6.3 %	1.1 %	92.4 %	0.2 %
$V_s =$ 8 km/s	23.2 %	10.8 %	64.2 %	1.8 %
$V_s =$ 10 km/s	42.5 %	10.9 %	41.3 %	5.4 %
$V_s =$ 12 km/s	52.1 %	13.4 %	31.5 %	3.0 %

to that of the initial state. This is contrary the information shown in Fig. 5, in which the thermodynamic parameters only differ from the initial state after 0.2 ps. These results also suggest that the electron structure is more sensitive to shock wave compression. Meanwhile, Fig. 8 shows that as the compression proceeds with time, the contribution proportion of Cu atoms is consistent with the contribution proportion of D orbital, and the contribution proportion of Al atoms is consistent with the contribution proportion of P orbital. It suggests that the contribution proportion of P orbital of the crystal is mainly due to the P orbital of Al atoms, while the contribution proportion of D orbital of the crystal is mainly due to the D orbital of Cu atoms.

Compared to the case of 8 km/s, the contribution proportion from different kinds of atoms in the cases of 10 km/s and 12 km/s show a similar variation with time, but with a larger fluctuation after 0.2 ps, as shown in Fig. 8. The shock wave speed has the greatest influence on the contribution proportion of Cu and Al atoms. For example, the larger the shock speed, the smaller the contribution proportion of Cu atoms and the larger the contribution proportion of Al atoms after shock. Especially, at the shock speed of 12 km/s, the crystal orbital is mainly contributed by S orbital with a contribution proportion of 44.5 %. Correspondingly, with the increase of the shock speed, the crystal orbital is more and more contributed by Al atoms. Of course, the contribution proportion of Cu atoms is also important, which makes D orbital still important for the crystal orbital. The variation of the contribution proportion of different kinds of orbitals also suggests that some electrons undergo orbital transition during the compression process. An *iso*-surface diagram of the electron cloud of occupied orbital No. 300 is shown in Fig. 9, where the electron cloud with blue colour and red colour represents a negative and positive *iso*-surface, respectively. It is interesting that the electron cloud of Cu atoms presents a typical shape of D orbital, i.e. cross dumbbell/peanut, as shown in the enlarged snapshots in Fig. 9(b). It agrees well with Table 4 and Table 5, which demonstrates that D orbital is mainly contributed by Cu atoms. It should be noted that compared to Cu and Al atoms, the contribution proportion from Li and
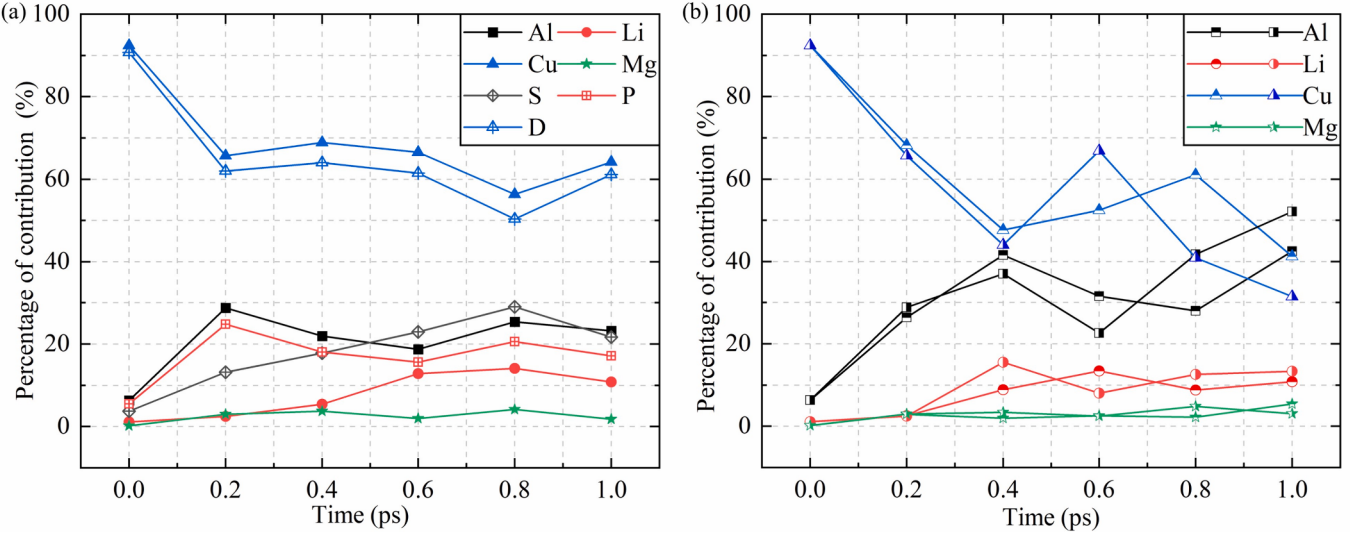
Fig. 8. Variation of contribution proportion of crystal orbital with time at No. 300 occupied orbital: (a) shock speed of 8 km/s; (b) shock speed of 10 km/s (semi-open symbol with top solid) and 12 km/s (semi-open symbol with right solid).
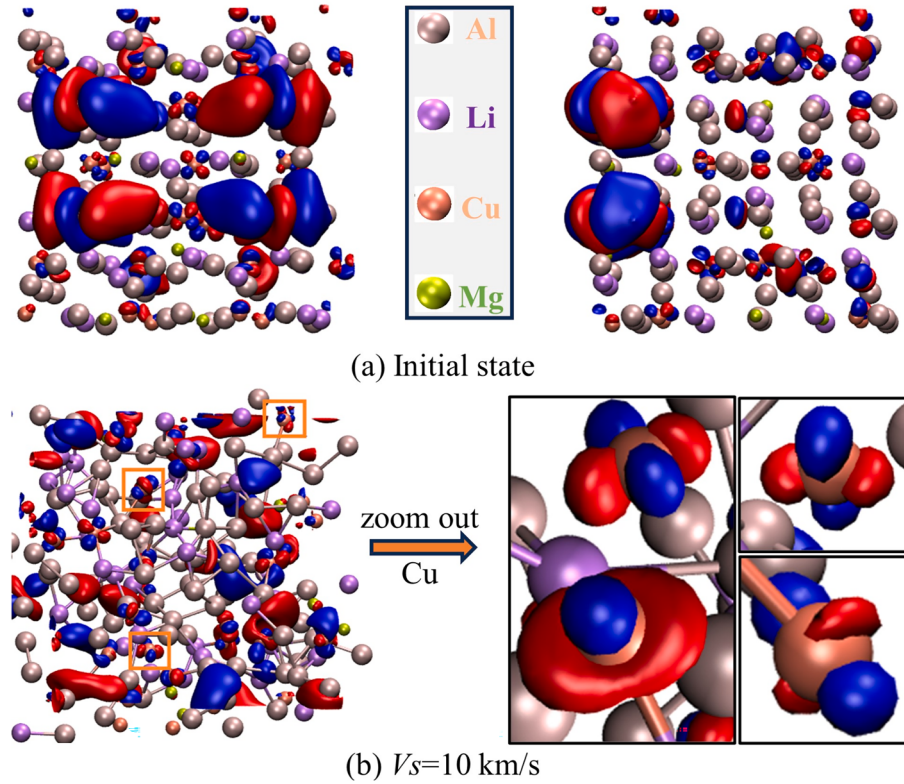

Fig. 9. Iso-surface diagram of the electron cloud of No. 300 occupied orbital: (a) initial state (left: X-Z plate, right: Y-Z plane); (b) shock speed of 10 km/s (left: Y-Z plane, right: Cu atoms).

Mg atoms are much smaller also less sensitive to the shock wave speed in all cases.

To further illustrate the mechanics of the electronic structure in the shock compression process, the evolution of the Total Density of States (TDOS) and Projected Density of States (PDOS) with time at the shock speed of 8 km/s is shown in Fig. 10, where the vertical black dotted line represents Fermi energy level at absolute 0 K, and the vertical red dotted line represents the energy of No. 300 occupied orbital used in above analysis. It could be found that the electronic distribution of the crystal is mainly in the occupied state at different time, in which TDOS is mainly

contributed by the energy less than the Fermi energy level. In the occupied state, the PDOS of Cu atoms is close to the TDOS, and the contribution of Cu is basically from its D orbital contribution, especially before 0.2 ps. It indicates that TDOS is mainly contributed by Cu atoms, which agree with the information presented by the energy level at the occupied orbitals. Meanwhile, TDOS is close to the PDOS of Al atoms for the energy larger than the Fermi energy level, demonstrating that TDOS is mainly contributed by Al atoms in the non-occupied state. Similarly, the most contribution of Al comes from its P orbital contribution. At the initial state, as shown in Fig. 10(a), Cu atoms have a large peak at − 4.2
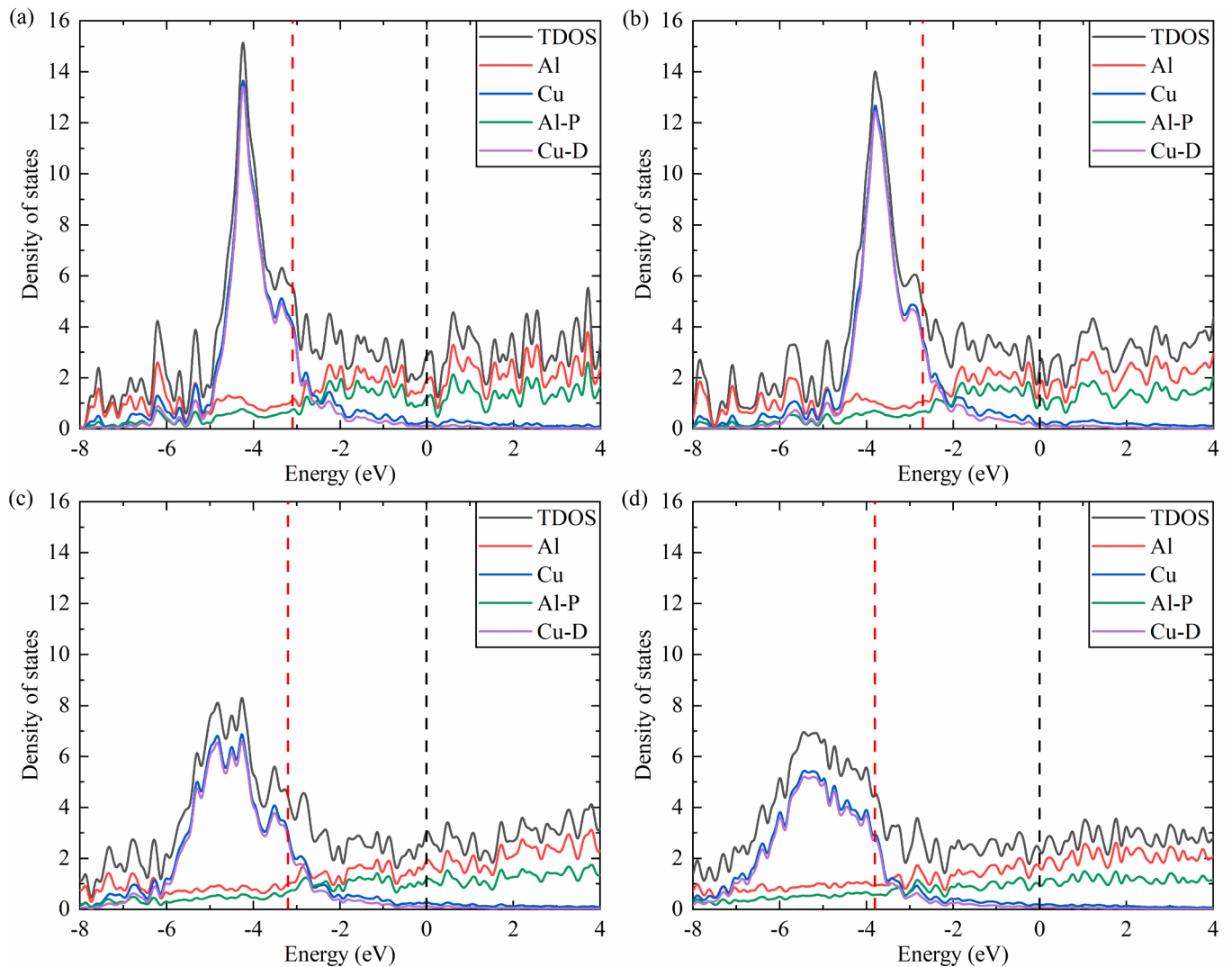
Fig. 10. Total Density of States (TDOS) and Projected Density of State (PDOS) at different times with shock speed of 8 km/s, including Al atoms, Cu atoms, P orbital of Al atoms, D orbital of Cu atoms: (a) $t = 0$ ps, (b) $t = 0.2$ ps, (c) $t = 0.4$ ps and (d) $t = 1$ ps, in which the red dotted line represents the energy of No. 300 occupied orbital, and the black dotted line represents Fermi energy level.

eV with a span of $- 5.0 \sim - 3$ eV. As the compression proceeds, the peaks of both TDOS and the PODS of Cu atoms decrease with time, especially during the interval of 0.2–0.4 ps, but the corresponding span increases, which is significantly observed from Fig. 10(b)-(d). This trend is also observed for the cases with the shock speed of 10 km/s and 12 km/s, as shown in the supplementary materials. Compared to the case of with the shock speed of 8 km/s, the transition from significant peaks to relative flat distribution occurs at earlier time. For example, at the shock speed of 12 km/s, there are no obvious peaks even at 0.4 ps, Meanwhile, the overlapping region of PDOS of Al and Cu atoms increases with the increase of the shock speed, which increases the likelihood of the formation of metallic bonds between them.

The total charge number of each kind of atom is shown in Table 6, for which the SPCA method is used. At the initial state, the Al, Li and Mg atoms have positive charges. The Al atoms have the largest positive charge number with a value of 69.7C, while the Cu atoms have a negative charge with the value of -91.6C. At the final thermodynamic state at the shock speed of 8 km/s, the total charge number of Li atoms decreases to negative, with a value of -103.7C, while the total charge number of Cu atoms change to positive. With the increase of the shock speed, the total charge number at final thermodynamic state carried by Al atoms becomes smaller, and it is even negative at the shock speed of 12 km/s, while the total charge carried by Cu atoms increases. These results suggest that during the shock compression process, the electrons of Cu atoms tend to be transferred to Li atoms and Al atoms. It should be noted that the charges of atoms are not uniform, which could be found in Fig. 11. By comparing Fig. 11 with the spatial positions of atoms shown in Fig. 6, it is clear that even for the same kind of atoms, some atoms have positive charges, while others may have negative charges.

4. Conclusions

The dynamic response process of shock wave impact on single crystal aluminium and aluminium-rich multicomponent alloy Al-Cu-Li-Mg is simulated by using the combination of Ab initio Molecular Dynamics

Table 6
Total number of atomic charges carried by different atoms in the Al-Li-Cu-Mg alloy.

Charges (C)	Al	Li	Cu	Mg
Initial state	69.7	13.0	−91.6	8.9
$V_s = 8$ km/s	93.1	−103.7	7.8	2.8
$V_s = 10$ km/s	20.2	−105.8	80.8	4.8
$V_s = 12$ km/s	−25.6	−117.8	132.1	11.3
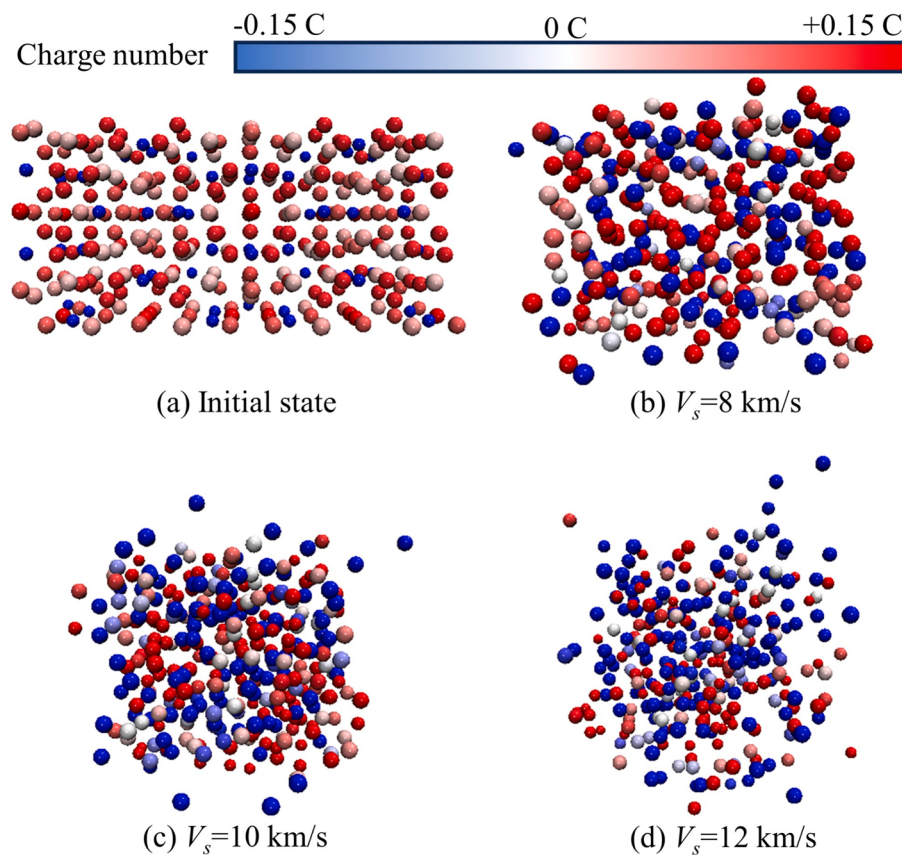
Fig. 11. Atomic charges distribution of atoms at the initial state and the final thermodynamic state of different shock speeds: (a) initial state, (b) $V_s = 8$ km/s, (c) $V_s = 10$ km/s and (d) $V_s = 12$ km/s.

(AIMD) and Multi-Scale Shock Technique (MSST). The simulation is verified by comparing the particle velocity of single crystal obtained in this work with the data in literature. This is followed the analysis the dynamics of shock compression process, atomic migration trajectories and electron structures. Main results from this work are summarised as follows.

1) Two stages could be found in the shock compression process: oscillatory compression of the crystal cell and oscillatory migration of the atoms. The shock compression process not only involves the migration of atoms, but also is related to electronic transition. The compression at high shock speed would lead to the vaporisation of the crystal.

2) For single crystal aluminium, the disordered structure could only be induced at high shock speed. For multicomponent alloy Al-Cu-Li-Mg, the structure of crystal cell can be disordered even at low shock speed, due to the difference in the ability of migration between different kinds of atoms. Some atoms migrate outside the crystal cell, especially for aluminium and lithium atoms.

3) As the multicomponent alloy Al-Cu-Li-Mg alloy is compressed, the contribution proportion of crystal orbital shows a sharp decrease for D orbital, while it increases significantly for S orbital and P orbital. With the increase of the shock speed, the energy levels are more and more contributed by Al atoms, which is mainly due to the transition of the electrons of Al atoms from low to high crystal orbitals.

4) Total Density of States (TDOS) is mainly contributed by the Projected Density of State (PDOS) of Cu atoms in the occupied state of energy levels, while it is close to the PDOS of Al atoms in the non-occupied state of energy levels. The overlapping region of PDOS of Al and Cu atoms increases with the increase of the shock speed, which affects the formation of metallic bonds between them.

CRediT authorship contribution statement

Yulun Xu: Writing – original draft, Visualization, Methodology, Investigation, Formal analysis. **Wenguang Nan:** Writing – review & editing, Writing – original draft, Visualization, Supervision, Methodology, Investigation, Funding acquisition, Formal analysis, Conceptualization. **Zhonggang Sun:** Supervision, Funding acquisition.

Declaration of competing interest

The authors declare that they have no known competing financial interests or personal relationships that could have appeared to influence the work reported in this paper.

Data availability

Data will be made available on request.

Acknowledgements

Appendix A. Supplementary data

Supplementary data to this article can be found online at https://doi.org/10.1016/j.commatsci.2024.113268.

References

[1] J. Chen, X. Zhou, W. Wang, B. Liu, Y. Lv, W. Yang, D. Xu, Y. Liu, A review on fundamental of high entropy alloys with promising high–temperature properties, J. Alloy. Compd. 760 (2018) 15–30.

[2] M. Du, B. Liu, Y. Liu, Y. Yang, Dynamic behavior of additively manufactured FeCoCrNi high entropy alloy, Metals 13 (2022).

[3] Y. Tang, D.Y. Li, Dynamic response of high-entropy alloys to ballistic impact, Sci. Adv. 8 (2022).

[4] W. Dong, Z. Zhou, M. Zhang, Y. Ma, P. Yu, P.K. Liaw, G. Li, Applications of high-pressure technology for high-entropy alloys: a review, Metals 9 (2019).

[5] Y. Mu, Z. Wu, Y. Ma, Y. Jia, D. Yang, P. Ma, W. Zhao, D. Li, Y. Jia, G. Wang, T. Chang, Shock-compression microstructure transformation of the additive manufactured FeCoNiAlTi high-entropy alloy, Vacuum 217 (2023).

[6] H. Xie, Z. Ma, W. Zhang, H. Zhao, L. Ren, Amorphization transformation in high-entropy alloy FeNiCrCoCu under shock compression, J. Mater. Sci. Technol. 175 (2024) 72–79.

[7] N.B. Zhang, J. Xu, Z.D. Feng, Y.F. Sun, J.Y. Huang, X.J. Zhao, X.H. Yao, S. Chen, L. Lu, S.N. Luo, Shock compression and spallation damage of high-entropy alloy Al0.1CoCrFeNi, J. Mater. Sci. Technol. 128 (2022) 1–9.

[8] H. Li, C. Shao, O.K. Orhan, D.F. Rojas, M. Ponga, J.D. Hogan, Strain-rate-dependent mechanical behavior of a non-Equimolar CoCrFeMnNi high entropy alloy with a segmented coarse grain structure, Materialia 21 (2022).

[9] Y. Qi, M. Zhao, M. Feng, Molecular simulation of microstructure evolution and plastic deformation of nanocrystalline CoCrFeMnNi high-entropy alloy under tension and compression, J. Alloy. Compd. 851 (2021).

[10] B. Wang, X. Huang, A. Fu, Y. Liu, B. Liu, Serration behavior and microstructure of high entropy alloy CoCrFeMnNi prepared by powder metallurgy, Mater. Sci. Eng. A 726 (2018) 37–44.

[11] H. Li, C. Shao, D.F. Rojas, M. Ponga, J.D. Hogan, Micro-hardness and strain-rate-dependent compressive response of an ultra-light-weight Mg-Li-Al alloy, J. Alloy. Compd. 890 (2022).

[12] X. Yang, S. Xu, L. Liu, The shock response and spall mechanism of Mg–Al–Zn alloy: molecular dynamics study, Acta Mech. Solida Sin. 35 (2022) 495–503.

[13] Z. Xie, W.-R. Jian, S. Xu, I.J. Beyerlein, X. Zhang, Z. Wang, X. Yao, Role of local chemical fluctuations in the shock dynamics of medium entropy alloy CoCrNi, Acta Mater. 221 (2021).

[14] B. Liu, Z. Jian, L. Guo, X. Li, K. Wang, H. Deng, W. Hu, S. Xiao, D. Yuan, Effect of crystallographic orientations on shock-induced plasticity for CoCrFeMnNi high-entropy alloy, Int. J. Mech. Sci. 226 (2022).

[15] J.A. Stewart, J.K. Startt, R. Dingreville, A molecular dynamics study on the Mie-Grüneisen equation-of-state and high strain-rate behavior of equiatomic CoCrFeMnNi, Materials Res. Lett. 11 (2023) 1055–1062.

[16] L. Zhao, H. Zong, X. Ding, T. Lookman, Anomalous dislocation core structure in shock compressed bcc high-entropy alloys, Acta Mater. 209 (2021).

[17] Y. Huang, Y. Xiong, P. Li, X. Li, S. Xiao, H. Deng, W. Zhu, W. Hu, Atomistic studies of shock-induced plasticity and phase transition in iron-based single crystal with edge dislocation, Int. J. Plast 114 (2019) 215–226.

[18] B. Chen, Y. Li, D. Şopu, J. Eckert, W. Wu, Molecular dynamics study of shock-induced deformation phenomena and spallation failure in Ni-based single crystal superalloys, Int. J. Plast 162 (2023).

[19] E.J. Reed, L.E. Fried, J.D. Joannopoulos, A method for tractable dynamical studies of single and double shock compression, Phys Rev Lett 90 (2003) 235503.

[20] X. Chen, S. Li, X. Tang, S. Lu, Y. Zhao, T. Fu, X. Peng, Molecular dynamics analysis of the low-temperature shock behavior of the CoCrFeMnNi high-entropy alloy, Model. Simul. Mater. Sci. Eng. 30 (2022).

[21] Y. Hu, Y. Wang, G. Yang, X. Liu, H. Huang, Shock Hugoniot of an equiatomic high-entropy alloy NbMoTaW up to 143 GPa, J. Appl. Phys. 134 (2023).

[22] S.K. Singh, A. Parashar, Shock resistance capability of multi-principal elemental alloys as a function of lattice distortion and grain size, J. Appl. Phys. 132 (2022).

[23] W. Li, S. Chen, Z. Aitken, Y.-W. Zhang, Shock-induced deformation and spallation in CoCrFeMnNi high-entropy alloys at high strain-rates, Int. J. Plast 168 (2023).

[24] J. Chen, W. Chen, S. Chen, G. Zhou, T. Zhang, Shock Hugoniot and Mie-Grüneisen EOS of TiAl alloy: a molecular dynamics approach, Comput. Mater. Sci 174 (2020).

[25] C.J. Mundy, A. Curioni, N. Goldman, I.F. Will Kuo, E.J. Reed, L.E. Fried, M. Ianuzzi, Ultrafast transformation of graphite to diamond: an ab initio study of graphite under shock compression, J. Chem. Phys. 128 (2008) 184701.

[26] Z.L. Liu, X.L. Zhang, L.C. Cai, Shock melting method to determine melting curve by molecular dynamics: Cu Pd, and Al, J. Chem. Phys. 143 (2015) 114101.

[27] A. Neogi, N. Mitra, A metastable phase of shocked bulk single crystal copper: an atomistic simulation study, Sci. Rep. 7 (2017) 7337.

[28] P. Hohenberg, W. Kohn, Inhomogeneous electron gas, Phys. Rev. 136 (1964) B864–B871.

[29] W. Kohn, L.J. Sham, Self-consistent equations including exchange and correlation effects, Phys. Rev. 140 (1965) A1133–A1138.

[30] T.D. Kuhne, M. Iannuzzi, M. Del Ben, V.V. Rybkin, P. Seewald, F. Stein, T. Laino, R. Z. Khaliullin, O. Schutt, F. Schiffmann, D. Golze, J. Wilhelm, S. Chulkov, M. H. Bani-Hashemian, V. Weber, U. Borstnik, M. Taillefumier, A.S. Jakobovits, A. Lazzaro, H. Pabst, T. Muller, R. Schade, M. Guidon, S. Andermatt, N. Holmberg, G.K. Schenter, A. Hehn, A. Bussy, F. Belleflamme, G. Tabacchi, A. Gloss, M. Lass, I. Bethune, C.J. Mundy, C. Plessl, M. Watkins, J. VandeVondele, M. Krack, J. Hutter, CP2K: An electronic structure and molecular dynamics software package - Quickstep: efficient and accurate electronic structure calculations, J. Chem. Phys. 152 (2020) 194103.

[31] W. Humphrey, A. Dalke, K. Schulten, VMD: visual molecular dynamics, J. Molec Graphics 14 (1996) 33–38.

[32] T. Lu, F. Chen, Multiwfn: a multifunctional wavefunction analyzer, J. Comput. Chem. 33 (2012) 580–592.

[33] T. Lu, F. Chen, Calculation of molecular orbital composition, Acta Chim. Sinica 69 (2011) 2393–2406.

[34] S. Grimme, Density functional theory with London dispersion corrections, WIREs Comput. Mol. Sci. 1 (2011) 211–228.

[35] J. Grafenstein, D. Cremer, An efficient algorithm for the density-functional theory treatment of dispersion interactions, J. Chem. Phys. 130 (2009) 124105.

[36] S. Grimme, J. Antony, T. Schwabe, C. Muck-Lichtenfeld, Density functional theory with dispersion corrections for supramolecular structures, aggregates, and complexes of (bio)organic molecules, Org. Biomol. Chem. 5 (2007) 741–758.

[37] H. Schroder, J. Huhnert, T. Schwabe, Evaluation of DFT-D3 dispersion corrections for various structural benchmark sets, J. Chem. Phys. 117 (2017) 044115.

[38] H. Schroder, A. Creon, T. Schwabe, Reformulation of the D3(Becke-Johnson) dispersion correction without resorting to higher than C(6) dispersion coefficients, J. Chem. Theory Comput. 11 (2015) 3163–3170.

[39] D. Marx, J. Hutter, Ab initio molecular dynamics: basic theory and advanced methods, Cambridge University Press, New York, 2009.

[40] N. Pavlyuk, G. Dmytriv, V. Pavlyuk, B. Rozdzynska-Kielbik, G. Cichowicz, M. K. Cyranski, I. Chumak, H. Ehrenberg, New cubic cluster phases in the Mg-Ni-Ga system, Acta Crystallogr B Struct. Sci. Cryst Eng. Mater 76 (2020) 534–542.

[41] A.C. Mitchell, W.J. Nellis, J.A. Moriarty, R.A. Heinle, N.C. Holmes, R.E. Tipton, G. W. Repp, Equation of state of Al, Cu, Mo, and Pb at shock pressures up to 2.4 TPa (24 Mbar), J. Appl. Phys. 69 (1991) 2981–2986.

[42] D. Choudhuri, Y.M. Gupta, Shock compression and unloading response of 1050 aluminum to 70 GPA, AIP Conf. Proc. (2012) 755–758.

[43] X. Yang, X. Zeng, C. Pu, W. Chen, H. Chen, F. Wang, Molecular dynamics modeling of the Hugoniot states of aluminum, AIP Adv. 8 (2018).

[44] Y. Ju, Q. Zhang, Z. Gong, G. Ji, L. Zhou, Molecular dynamics simulation of shock melting of aluminum single crystal, J. Appl. Phys. 114 (2013).

[45] W.J. Nellis, J.A. Moriarty, A.C. Mitchell, M. Ross, R.G. Dandrea, N.W. Ashcroft, N. C. Holmes, G.R. Gathers, Metals physics at ultrahigh pressure: aluminum, copper, and lead as prototypes, Phys Rev Lett 60 (1988) 1414–1417.

[46] I.V. Lomonosov, Multi-phase equation of state for aluminum, Laser Part. Beams 25 (2007) 567–584.